Ultimate shear response of ultra-high-performance steel fibre-reinforced concrete elements

C. Țibea[1] · Dan V. Bompa[2]

Abstract

This paper examines the experimental performance of ultra-high-performance steel fibre-reinforced concrete (UHPSFRC) beams subjected to loads at relatively low shear span-to-depth ratios. The results and observations from six tests provide a detailed insight into the ultimate response including shear strength and failure mode of structural elements incorporating various fibre contents. The test results showed that a higher fibre content results in an increase in ultimate capacity and some enhancement in terms of ductility. Detailed nonlinear numerical validations and sensitivity studies were also undertaken in order to obtain further insights into the response of UHPSFRC beams, with particular focus on the influence of the shear span-to-depth ratio, fibre content and flexural reinforcement ratio. The parametric investigations showed that a reduction in shear span-to-depth ratio results in an increase in the member capacity, whilst a reduction in the flexural reinforcement ratio produces a lower ultimate capacity and a relatively more flexible response. The test results combined with those from numerical simulations enabled the development of a series of design expressions to estimate the shear strength of such members. Validations were performed against the results in this paper, as well as against a collated database from previous experimental studies.

Keywords Ultra-high-performance steel fibre-reinforced concrete · Shear strength · Nonlinear simulations · Concrete damage plasticity · Parametric investigations

1 Introduction

Ultra-high-performance concrete (UHPC) exceeds the performance of normal or high-strength concrete, allowing for the construction of more slender and efficient reinforced concrete (RC) structures. This is achieved using ultra-fine constituents and reactive powders which improve the mechanical properties and durability, yet increases the brittleness [1, 2]. For enhancement of the ductility properties, steel fibres are particularly attractive as concrete constituents [2–4]. These also can contribute to reducing the amount and congestion of conventional reinforcement in RC elements [4, 5] and are widely used in practice in tunnel linings, industrial floor slabs and aircraft runways. UHPC is a low water-to-binder ratio cementitious composite that has compressive strengths in the range of 130–160 MPa, under ambient curing and typical mixing technology. It has a low porosity due to improved homogeneity and enhanced packing density due to the use of relatively fine and ultra-fine materials such as micro- or nano-silica [6]. In UHPC, the coarse aggregates are replaced by fine sand and quartz powders, as in high-strength cement pastes, the skeleton formed by the conventional aggregates can become the weakest component [7].

High-strength mixes provided with micro-silica tend to have a denser microstructure in comparison with conventional mixes due to the formation of the new gel as a result of the secondary hydration between the calcium hydroxide and silica [1, 6]. Under complex and controlled curing regimes and production techniques, such UHPC can reach strengths above 450 MPa [8]. Silica fume, in ranges up to 25–30% of the cement mass along with heat treatment, increases C–S–H production through accelerating the cement hydration, as well as acts as a micro-filler of concrete voids to reduce the porosity [9]. Aiming at reducing the environmental impact

✉ Dan V. Bompa
  d.bompa@surrey.ac.uk

1   StruSoft AB, Malmö, Sweden

2   Department of Civil and Environmental Engineering, University of Surrey, Guildford GU2 7XH, UK

of UHPC, which uses at least twofold of the cement used in normal-strength concrete, recent studies substituted cement up to about 45% by weight by less-energy-intensive cementitious additives such as fly ash, ground granulated blast-furnace slag, limestone powder or metakaolin [2, 10].

Steel fibre-reinforced concrete (SFRC) is a composite material that is characterised by an enhanced ductility and post-cracking tensile residual strength or toughness, due to the reinforcement mechanisms provided by fibres bridging the crack surfaces [11, 12]. The mechanical performance of UHPSFRC of cement-based composites is strongly affected by the fibre volume, fibre geometry and orientation within the matrix. Tensile, bending and compressive cracking stress, peak stress, strain at peak stress, toughness and residual strength under cyclic loading are significantly improved with the increase in volumetric fibre content [11, 13]. For the same fibre content, twisted steel fibres lead to a better mechanical performance than hooked-end fibres [14], and implicitly hooked fibres are more effective than the straight geometries. Besides enhanced ductility and spalling properties, there is a significant benefit of using steel fibres in concrete structures where shear or punching shear is a governing consideration in design [15, 16]. The results showed that incorporating a high dosage of fibres (0.75–1.25% in volume) into concrete significantly improves the structural behaviour of SFRC beams; this provides bending hardening, considerably limits crack opening in service and gives a ductile behaviour for ultimate conditions [4]. An increase in steel fibre volume fraction from 0.5 to 0.75% increased the shear capacities by 13% and 30%, respectively, and the diagonal cracking strength by 35% on average [17]. Even a relatively low amount of fibres, below 0.7%, can contribute to the shear strength and ductility of concrete beams without transverse reinforcement [5].

UHPSFRC experimental member studies typically focused on the flexural response of rectangular beams provided with conventional longitudinal reinforcement in low or high amounts and typically incorporating transverse reinforcement [18–21]. In terms of benefits, the presence of fibres had a similar effect as for normal or high-strength concrete. An increase in steel fibre content generally produces lower shear crack widths and a less brittle behaviour [22]. A moderate number of stirrups can effectively restrain shear cracks and allow more parallel diagonal shear cracks to develop and propagate thoroughly within the shear span [23–25]. Shear performance of UHPSRFC was addressed through a limited number of push-off tests [22], T-beams [23, 24] and I-beams with and without openings within the shear span [25]. Numerical simulations of UHPFRC behaviour using nonlinear procedures are limited to modelling the material response [26–28] or the flexural response RC beams incorporating UHPFC materials [19, 29]. Although shear behaviour was successfully represented using three-dimensional models for conventional RC beams and slabs [e.g. 30], models incorporating UHPSFRC seem to be lacking.

This paper presents a study into the response of UHPSFRC materials and elements through a series of compressive and flexural tests on cubic and prismatic samples, respectively, as well as on medium-scale I-beams provided with conventional longitudinal reinforcement and various steel fibre contents. After describing the experimental methodology and test results, nonlinear numerical validation procedures and parametric studies are carried out against flexural samples and structural beams, using concrete damage plasticity models. An inverse analysis is carried out to assess the tensile stress–strain curve of UHPSFRC, which is used for modelling the structural members. The results from the numerical simulations along with those from the tests in this paper and from a collated database are used for the modification of a shear strength assessment method for UHPSFRC members with particular focus on beams loaded within low values of shear span-to-depth ratios. The proposed method is shown to offer a reliable and practical approach for shear strength assessment of structural UHPSFRC members.

2 Experimental assessment

2.1 Materials and mix designs

The concrete mixes incorporated cement silica fume, quartz, admixtures and tap water. The binders include CEM I 52.5 R cement with high initial strength conforming to BS EN 197-1 [31] and a high SiO_2 content silica fume. The cement composition included on around 95% main clinker components (tricalcium silicate C_3S, dicalcium silicate C_2S, tricalcium aluminate C_3A and tetracalcium aluminoferrite C_4AF), < 4% sulphates SO_3, < 0.10% chlorides Cl, < 0.9% alkali Eq Na_2O. The silica fume was added to improve internal cohesion and water retention in the fresh concrete, as well as to facilitate particle packing for increasing the cement matrix density and strength due to the formation of additional hydration products in hardened concrete [32]. Quartz sand particles with sizes up to 1.2 mm and with a specific gravity of 2.65 were used as mineral aggregates. A polycarboxylate ether superplasticiser was used to improve workability and ensure suitable flow ability whilst maintaining low water-to-binder ratio in the range of $w/b \approx 0.13$ [33]. Its main effect is accelerating cement hydration through an earlier development of hydration heat and rapid development of hydration products.

The concrete mixes investigated in this paper incorporated two fibres with two relative configurations. Longer hooked-end fibres with a length of $l_f = 25$ mm and a diameter of $d_f = 0.4$ mm were used stand-alone or mixed in a 50/50

ratio with shorter straight fibres with a length of $l_f = 6$ mm and a diameter of $d_f = 0.175$. The benefit of adding two types of fibres in the cementitious matrix is that these act at two different scales that would enhance the mechanical properties and post-cracking performance of SFRC. The longer fibres were made of stainless steel and had nominal tensile strengths above 1450 MPa and elastic modulus around 210 GPa [34]. The shorter fibres were relatively stronger with a tensile strength above 2800 MPa and a similar elastic modulus as the longer fibres. These were made of steel with a brass coating of about 8.5 g/m^2 [35]. These fibres were mixed in the cementitious matrix comprising the above materials in three fibre percentages by volume V_f: 1.5%, 2.0% and 2.55%. The mixes incorporating the longer fibres ($l_f/d_f = 62.5$) are noted with L, whilst those which include both long ($l_f/d_f = 62.5$) and short ($l_f/d_f = 34.3$) fibres are referred to as hybrid and noted with H.

The cement, silica fume and quartz sand, in the ratios listed in Table 1, were mixed together in an 85-L rotary mixer, until a homogenous dry mix was obtained. Following, the water combined with the admixture was mixed together until an acceptable level of workability was reached. Ultimately, the fibres (L) or the fibre blend (H) were integrated in the wet mix and mixed together. Each concrete batch required up to 10–15 min total mixing time to be completed.

Concrete fresh properties were assessed by means of a flow cone, and it was shown that steel fibres did not influence significantly the flow, which was around 120 mm for all mixes. Cubic samples of 50, 70, 100 mm, along with $100 \times 100 \times 400$ mm prismatic samples, were prepared to assess the compressive and flexural strength of the investigated concrete materials. The material strengths are listed in Table 2. The concrete poured in the larger specimens prepared for structural shear testing was produced in the same manner as for the samples for material testing.

The concrete prisms and structural members were cast horizontally with the bottom fibre on the bed of the formworks. After casting, all concrete elements were covered with a thin oil film and plastic sheets to prevent evaporation and ensure appropriate hydration. The specimens were removed from forms 24 h after casting and further subjected to a steam curing regime at 90 °C and 40% relative humidity for a period of 5 days. The structural members were provided with Grade S500 longitudinal reinforcement as described in the following section. The material properties of the steel reinforcement materials, determined from a minimum of three steel coupons, were the yield strength $f_y = 512$ MPa, the ultimate strength $f_t = 690$ MPa and the corresponding ultimate strain of $\varepsilon_u = 0.13$ mm/mm.

2.2 Specimens and testing arrangement

The parameters directly investigated in the testing programme were the fibre types, long or hybrid, as well as the steel fibre content (1.5%, 2.0% and 2.55%). Besides the cubic and prismatic samples cast for material strength assessment, six 1600 mm long structural members were tested. An I-shaped cross section with a maximum flange width of $b_f = 120$ mm and beam height of $h = 240$ mm was considered. The beam web had a thickness of $t_w = 50$ mm and a web height of $h_w = 60$ mm. The specimens were longitudinally reinforced with $2 \times \varnothing 14$ mm bars in tension and $2 \times \varnothing 10$ mm in compression. Except for $2 \times \varnothing 6$ bar used for fixing the longitudinal bars, at each of the supports, no transverse reinforcement was provided. The members were subjected to

Table 1 Concrete mixes

Concrete type	kg/m^3		
	2.55%	2.00%	1.50%
CEM 52.5R	1051	1051	1051
Silica fume	273	273	273
Aggregates 0–0.3 mm	265	271	277
Aggregates 0–0.63 mm	214	218	223
Aggregates 0.4–1.2 mm	168	172	176
Water	171	171	171
Superplasticiser	68	68	68
Steel fibres	200	157	118
w/b	0.129	0.129	0.129

Table 2 Specimen details

Configuration	$f_{c,cube}$ (MPa)			$f_{ct,fl}$ (MPa)	ρ_l (%)	d (mm)	a/d (–)	Fibre type*	V_f (%)
	50 mm	70 mm	100 mm						
CH25/1	183	158	148	22.6	1.15	223	1.25	H/H+S	2.55
CH20/1	185	167	150	–	1.15	223	1.25	H/H+S	2.00
CH15/1	165	154	136	21.4	1.15	223	1.25	H/H+S	1.50
CL25/1	189	161	154	24.8	1.15	223	1.25	L/H	2.55
CL20/1	187	166	155	–	1.15	223	1.25	L/H	2.00
CL15/1	173	151	138	23.5	1.15	223	1.25	L/H	1.50

*H/H+S, hybrid hooked end and straight; L/H, long hooked end; notations: $f_{c,cube}$, cube compressive strength; $f_{ct,fl}$, flexural strength; ρ_l, reinforcement ratio; a/d, shear span-to-depth ratio; V_f, fibre volume

monotonic three-point loading with a shear span-to-depth ratio (a/d) of 1.25 and were tested in two stages.

In the first Stage (1), the beams were supported at a moment span of $l_s = 1400$ mm with the load applied at $a/d = 1.25$ from the left support. After the ultimate state was reached, the undamaged side of the beam was supported at $l_s = 560$ mm and tested by applying the load mid-way between the supports (Stage 2). The specimen references depicted in Table 2 adopt the format $Cxyy/z$ in which x indicates the type of fibres (L for long and H for hybrid fibre blend), yy depicts the fibre volume (15 for 1.5%, 20 for 2.0% and 25 for 2.55%), and z is for the moment span configuration (1 for $l_s = 1400$ mm and 2 for $l_s = 560$ mm). For example, CH25/1 indicates a beam provided with hybrid fibre blend with a fibre content of 2.55% that had a moment span of 1400 mm. The concrete cover to the tension reinforcement was $c = 30$ mm. It is worth noting that, prior to carrying out tests in Stage 2, all specimens have been visually inspected within the short moment span $l_s = 560$ mm (Fig. 1b) using a crack width microscope. Except for CH20/2 which had some cracks within that region after being tested in Stage 1, all other specimens had no visible damage. Moreover, a few of the specimens (i.e. CH25/1, CH20/1, CL25/1 and CL20/1) had duplicates, yet for consistency, only one specimen per material type is reported in detail in this paper.
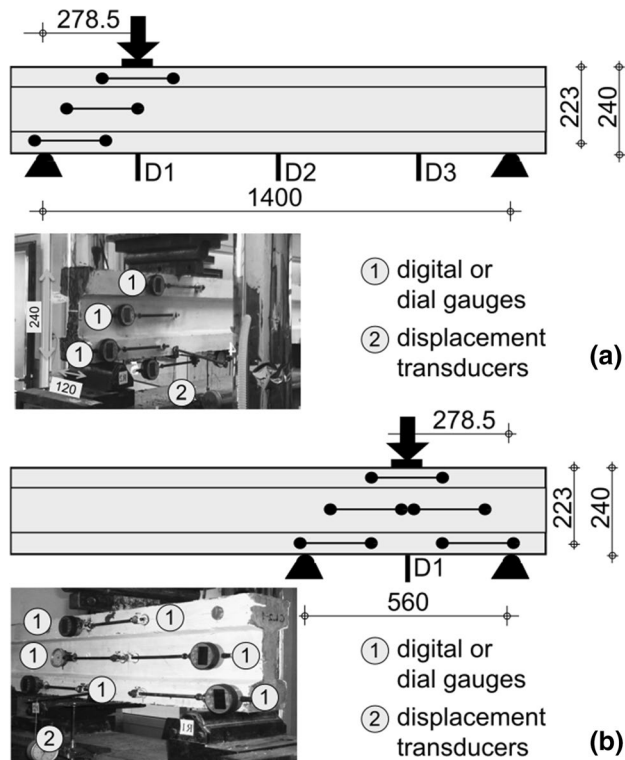

Fig. 1 Testing arrangement: **a** Stage 1 tests—$l_s = 1400$ mm, **b** Stage 2 tests—$l_s = 560$ mm

The test set-up was designed to simulate loading conditions characteristic for precast reinforced concrete (RC) beams under concentrated load with relatively high shear action. A schematic outline of the rig and instrumentation details are given in Fig. 1a, b. The load was applied through a hinge to the member by means of a hydraulic actuator that was provided with an HBM load cell with a capacity of 5 MN. The load was applied gradually in steps of 10 kN, and the data was recorded continuously throughout the test with a digital logger. Two steel rollers acting as boundary conditions were positioned on a stiff support frame which was connected directly to the laboratory floor. Displacements were measured at a minimum of three locations along with the moment span of the beam with transducers with a precision of 0.1 mm. The surface deformations were recorded at five locations by means of digital dial gauges within the shear span. These were positioned on the tension flange, web and compression flange of each specimen. Crack patterns and crack widths were recorded in all tests up to values of $w_{max} = 0.4$ mm. The mechanical properties of concrete were tested using a servo-hydraulic controlled testing machine type Advantest-9 with a capacity of 3000 kN, whilst those for assessment of the steel material properties through a testing machine provided with and 100 kN HBM load cell and HBM displacement measurement devices.

2.3 Test results

The tests described in this section focused on assessing the influence of fibre content and type to the shear performance of UHPSFRC elements. As mentioned before, concrete materials with relatively longer fibres with $l_f/d_f = 62.5$ or a fibre blend of long ($l_f/d_f = 62.5$) and short ($l_f/d_f = 34.3$) elements, with volumetric contents V_f of 1.5%, 2.0% and 2.55%, were used in the structural members. It is worth noting that a previous study on members subjected to shear action that incorporated similar concrete materials with 0% and 2.0% fibres showed that the presence of fibres increased the ultimate capacity of the fibrous concrete (UHPFRC) with up to twofold, and the corresponding ultimate displacement threefold in comparison the counterpart without fibres (UHPC) [36]. The same study indicated that the presence of 2.0% fibres increases the flexural strength with up to 150% of the non-fibre-reinforced concrete, whilst enhancing the post-peak response.

As shown in Fig. 2, the specimens tested in this paper had a shear-governed response, primarily due to the relatively short shear span-to-depth ratio. The test results depicted in Table 3 indicate a gradual increase in ultimate capacity with an increase in fibre content. For the members provided with hybrid fibre blend (CH), shear cracking was observed between 40 and 60 kN, corresponding to about 23–30% of the ultimate load, whilst flexural cracking initiated around
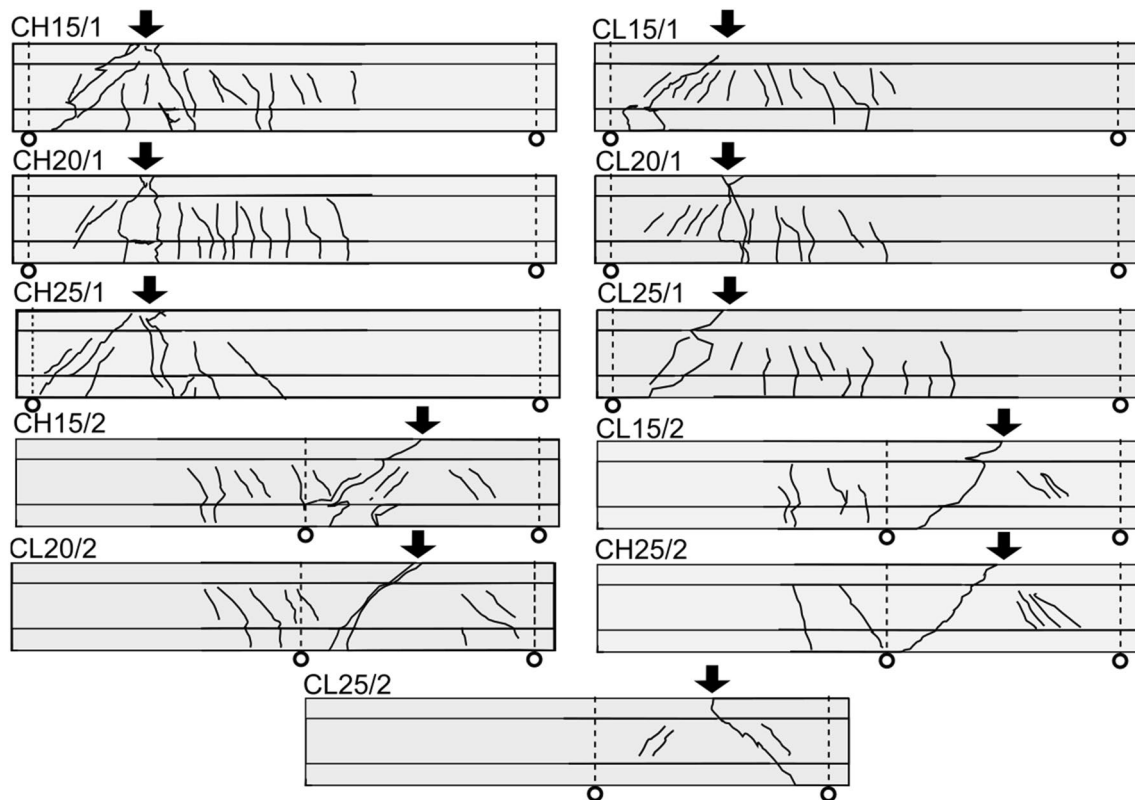
Fig. 2 Test crack patterns

Table 3 Test and numerical results

Configuration	P_{test} (kN)	P_{num} (kN)	P_{test}/P_{num} (−)
CH25/1	247	207	1.19
CH20/1	234	209	1.12
CH15/1	200	201	0.99
CL25/1	234	234	1.00
CL20/1	218	230	0.94
CL15/1	160	191	0.84
CH25/2	380	373	1.13
CH20/2	–	361	
CH15/2	330	349	0.95
CL25/2	380	405	0.94
CL20/2	354	403	0.88
CL15/2	280	390	0.72

Notations: P_{test}, test strength; P_{num}, strength from numerical simulations

70 kN which is in the range of expected cracking force based on the tensile concrete strengths obtained from material testing. Moreover, the specimen with the highest hybrid fibre blend (CH25/1) seems to have developed delayed cracking in comparison to the members with lower hybrid fibre blends (CH20/1 and CH15/1). Similarly, for members with long

steel fibres (CL), the shear cracking occurred between 40 and 71 kN which corresponds to 17–40% of the peak capacity. Flexural cracking was noted around 60 kN. It is worth noting that these values are based on a visual inspection and the crack widths corresponding to the force values mentioned above were in the range of $w = 0.02$ mm.

In terms of ultimate capacity, an increase in hybrid fibre blend content (V_f) from 1.5 to 2.0% showed an enhancement in strength 17% (CH15/1 vs. CH20/1), whilst an increase in V_f from 1.5 to 2.55% showed an increase in strength of about 24% (CH15/1 vs. CH25/1). An increase of 15% was observed between the CH15 and CH25 members with $V_f = 1.5\%$ and $V_f = 2.55\%$ subjected to concentrated load and short moment span ($l_s = 560$ mm). Based on the results from Table 3, it is noted that the hybrid fibre blend had a more beneficial effect in enhancing the ultimate capacity. Moreover, an increase in fibre volume from 1.5 to 2.0% showed an increase in capacity of about 34% (CL15/1 vs. CL20/1), whilst an increase in V_f from 1.5 to 2.55% showed a strength enhancement of about 46% (CL15/1 vs. CL25/1). For cases tested with short moment span ($l_s = 560$ mm), the strength enhancement was 27% and 36% for CL15/2 versus CL20/2, and CL15/2 and CL25/2, respectively.

As mentioned in Sect. 2.2, CH25/1, CH20/1, CL25/1 and CL20/1 had duplicates which were tested in the loading

arrangement illustrated in Fig. 1a. The standard deviation of the test strength of the two duplicates was 3.1%, 3.0%, 18%, 5.9% for CH25/1, CH20/1, CL25/1, CL20/1, respectively. Except for the strengths of the duplicates of CL25/1 which had relatively large standard variation, all results are within reliable limits.

More importantly, some increase in ultimate deformation was observed with an increase in fibre content. The beams provided with a fibre volume of 2.55% and 2.0% showed a flexurally governed shear failure, whilst those with 1.5% failed with limited or no sign of flexure. The increase in ductility is primarily attributed to the crack bridging effect provided by the fibres. This effect was clearly observed in the four point-bending tests on notched prismatic samples without longitudinal reinforcement, prepared for flexural strength assessment. Prisms with both long (CL) or hybrid (CH) fibre content of 2.55% had an increase of around 5.5% in strength in comparison with their counterparts with 1.5% fibre content (Table 2). Based on the experimental observations, the distribution of the two fibre types was relatively even through the failure surface, hence, contributing to a similar extent to the response. By contrast, non-homogenous distributions, either by localisation of the fibres depending on the casting direction or by bulging, would have an impact to the member capacity and would affect significantly the crack kinematics and crack bridging behaviour. The test results on prismatic samples are further used for inverse finite element analysis to obtain the uniaxial tensile constitutive response of UHPFRC. Such methods to assess the stress–stress response of concrete materials have been used before [e.g. 26, 37, 38].

3 Numerical modelling

3.1 Concrete damage plasticity

The 'concrete damaged plasticity' model (CDP), incorporated in the commercial finite element programme Abaqus 6.14 [39], was employed to represent the triaxial behaviour of concrete. For this, the potential yield function is controlled by the effective stress values, the biaxial behaviour of concrete ($f_{b0}/f_c = 1.16$) and $K_c = 2/3$ that governs the shape of the deviatoric plane. The CDP model accounts for a non-associated potential plastic flow, in which the plastic volume expansion is not proportional to the increase in stresses. This is represented in the plastic potential flow function by the dilation angle φ measured in the p–q plane at high confining pressure and the surface eccentricity ($\epsilon = 0.1$). The constitutive model requires uniaxial stress (σ)–strain (ε)/crack displacement (w)–damage (d_i) relationships for compression and tension behaviour. In this study, a plastic stiffness

degradation scheme, typical for coupled damage-plastic concrete constitutive models was adopted.

Before crushing in compression or cracking in tension, no degradation occurs, and the plastic strains are equal to the inelastic strains. Beyond these points, the stiffness reduction enables the development of irreversible plastic strains that are directly proportional to the stress decrease [30]. The damage in compression d_c and damage in tension d_t parameters are also part of the variable field output of the FE environment. They allow direct interpretation of the stress state within different regions of the members, illustrated by compression and tension damage patterns, and member stiffness degradation. Established on a continuum approach, in which no physical separation is created in the model mesh, tension damage mesh regions provide an effective way to illustrate the kinematic aspects of crack development. The input constitutive parameters have been determined based on the tests described in Sect. 2 and are presented next.

3.2 Uniaxial constitutive properties

As mentioned before, compression and four-point bending tests were performed to obtain the mechanical properties of the UHPFRC materials reported in this paper. The compression stress–strain curve obtained from tests was used as direct input in the numerical model, whilst the four-point bending tests were used to determine the tensile constitutive response. Assessment of direct tensile properties of steel fibre concrete materials requires a relatively complex testing arrangement. An alternative to assess the tensile stress–strain is through an indirect finite element analysis from three- or four-point bending tests. The procedure involves modelling the flexural test and carefully varying the key material parameters such as the tensile strength, fracture energy or post-peak representations and crack bandwidth to obtain close agreement between test and numerical force–crack mouth opening displacement curves [26, 37, 38]. It is assumed that a single straight crack transfers all stresses through the interface and the crack width varies linearly with its depth from mouth to root. The root of the crack with $w = 0$ represents the rotation point of two discrete bodies.

To simulate reliably the response of the flexural prismatic specimens, the full member geometry was accounted for in modelling. The models of $100 \times 100 \times 400$ mm samples constructed to undertake an inverse analysis for assessment of the tensile stress–strain curves of UHPFRC were made of 2D planar deformable shells incorporating four-node bilinear plane stress quadrilateral elements with reduced integration (CPS4R). Both 3D models using solid elements (C3D8R) and 2D models using the element types mentioned before have been built. Close inspection of the results indicated that both modelling procedures

offer nearly identical predictions and modelling prismatic members with square cross section can be regarded as plain stress problem. As a significant number of sensitivity studies need to be carried in order to obtain the tensile stress–strain from bending tests, a much lower computational time is obtained by employing shell models. This has been shown in past studies which indicated that both 3D solid and 2D shell modelling closely estimate the experimental load–deformation response of concrete members, with 2D modelling offering savings in the computational time of about 14-fold [40].

Additionally, besides the implicit computational time savings, this is also corroborated with the fact that a very fine mesh needs to be adopted in order to capture reliably the softening behaviour of concrete, as described below. Hence, shell models were used to address this particular problem. In the rectangular shell models, boundary conditions and load application points were made of circular discrete rigid wires connected to reference points and tied to the deformable shell component. The Newton–Raphson method was used for the integration procedure, and a displacement control procedure was considered in which a vertical displacement δ was applied to the relevant reference points.

The tensile strength of fibre-reinforced concrete is determined from the flexural strength obtained from four-point bending tests using an established model and a tensile-to-flexural strength conversion factor around $\alpha_{fl} \approx 0.6$ [41] (Eqs. 1–3). This parameter depends on the type of the stress–strain curve and implicitly type of concrete modelled [29]; hence, $\lambda_{fl} = 0.065$. In modelling, a linear-elastic behaviour was considered up to cracking f_{ct}, followed by a nonlinear tension softening law (Eq. 4) [42]. It is worth noting that the original softening law constitutive parameters ($c_1 = 3$, $c_2 = 6.93$, $w_{max} = 160$ µm) were calibrated against tests on normal concrete with tensile strengths around 3.2 MPa. A sensitivity analysis was carried out for the UHPSFRC materials investigated in this paper by modifying the c_1 and w_{max} parameters from Eq. 4 (Fig. 3). The c_1 parameter controls the shape of the descending branch, whilst w_{max} represents the crack opening at zero stress.

As mentioned before, the presence of steel fibres has a significant effect in enhancing the post-peak fracture energy, represented by the area under the tensile σ–ε curve. Implicitly, w_{max} for UHPSFRC depends on the fibre content and type, and it takes larger values than for normal concrete. In order to calibrate the nonlinear tension softening law, w_{max} of normal concrete (i.e. 160 µm) was multiplied with factors between 4.00 and 5.05, depending on the type of fibre and content (long fibres—L or hybrid blend—H; $V_f = 1.5$–2.55%) (Fig. 3a). On the other hand, the c_1 parameter was varied from 1 to 3. For the same w_{max}, a lower value of c_1 indicates lower fracture energy in comparison with a higher c_1 value (Fig. 3b).
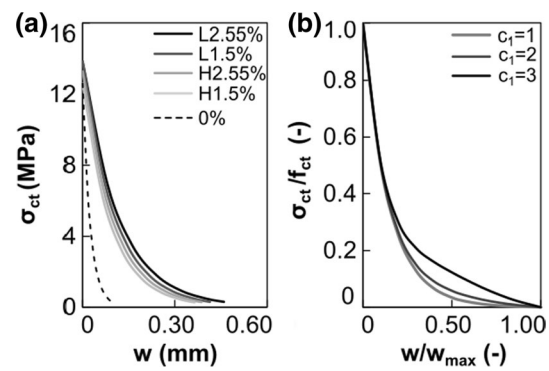
Fig. 3 Sensitivity analysis for the tensile stress–strain input curve: **a** influence of the ultimate crack width w_{max}, **b** influence of c_1 parameter

The sensitivity study showed that a value of $c_1 = 1$ captures reliably the test response. For the numerical input stress (σ), crack mouth displacement w_i–damage (d_t) relationships were considered. In the uniaxial post-peak tension regime, the damage is assumed to grow linearly from 0 to 0.9 which corresponds to $w = 0$ and w_{max}, respectively (Eq. 5). Such ranges were also employed in other studies from the literature [42]. Beyond this value, the damage scalar is subsequently held constant to preserve a residual stiffness and strength [43].

$$f_{ct,fl} = \frac{PL}{bh^2} \tag{1}$$

$$f_{ct} = \alpha_{fl} \times f_{ct,fl} \tag{2}$$

$$\alpha_{fl} = \frac{\lambda_{fl} \times h_b^{0.7}}{1 + \lambda_{fl} \times h_b^{0.7}} \tag{3}$$

$$\frac{\sigma}{f_{ct,num}} = \left\{ 1 + \left(c_1 \frac{w}{w_{max}} \right)^3 \right\} \exp\left(-c_2 \frac{w}{w_{max}} \right) \\ - \frac{w}{w_{max}} \left(1 + c_1^3 \right) \exp\left(-c_2 \right) \tag{4}$$

$$d_i = \begin{cases} 0 \rightarrow \varepsilon < \varepsilon_i \\ 1 - \sigma_i/f_{ci} \end{cases} \quad \text{where} \quad i = c, t. \tag{5}$$

An additional mesh sensitivity study was carried out to investigate the mesh size influence on the numerical response. Figure 4 shows the load–crack opening p–w curves for the models of the prismatic samples provided with four mesh sizes: 1.5 mm, 3 mm, 6 mm and 12 mm and 1.5% hybrid fibres (H1.5%). The crack width from numerical simulations has been obtained by subtracting the horizontal displacements at nodal points situated at
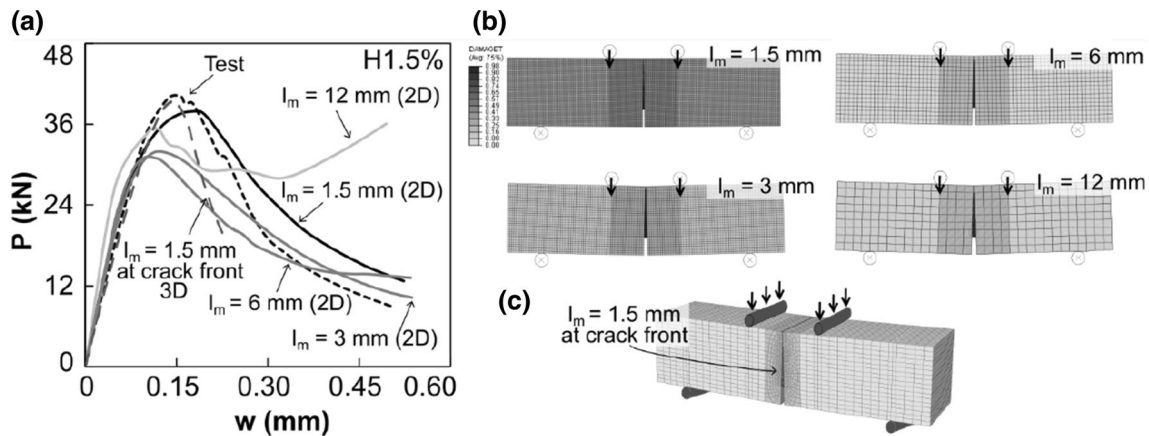
Fig. 4 Mesh sensitivity analysis for the inverse finite element analysis, **a** load–crack opening curves, **b** mesh sizes for 2D models, **c** 3D model

mid-depth of the two notch faces. This corresponds to the location of the displacement transducers attached to the test specimens. As observed, the mesh sizes equal to or higher than 3 mm offer lower strength and unreliable post-peak response, whilst the 1.5 mm mesh shows good agreement between the test and numerical response.

After validating the modelling procedures for the H1.5% concrete, the same approach was employed to the models with L1.5%, L2.55% and H2.55% concrete. For comparison purposes only, a three-dimensional model of H1.5% using solid elements (C3D8R) has been constructed (Fig. 4c). To reduce the computational time, only the crack front was meshed with 1.5 mm element seeds, whilst for the remaining model the mesh size was increased gradually. Even with this modelling strategy, the ratio between the computational time of the 3D model and the 2D model with $l_m = 1.5$ mm was higher by a factor of 127. As expected, both modelling techniques offer nearly identical results in terms of strength predictions.

The comparative test and numerical p–w curves are illustrated in Fig. 5, indicating a reliable modelling approach and that the tensile σ–ε obtained from the inverse analysis can be used for modelling of structural UHPFRC members. It is worth noting that for the intermediate fibre contents (L2.0% and H2.0%) the input tensile σ–ε was obtained from direct interpolation of σ–ε for materials with higher and lower fibre content. The compressive stress–strain σ–ε relationship was determined from material tests on cubic samples described in Sect. 2.1. A factor of 1.00 was used to convert 100 mm cube $f_{c,cube}$ to cylinder f_c compressive strength of UPHC, as suggested in studies from the literature [44]. Both structural and reinforcement steels were modelled using bilinear elastoplastic properties with hardening using the material properties obtained from material tests (Table 4).
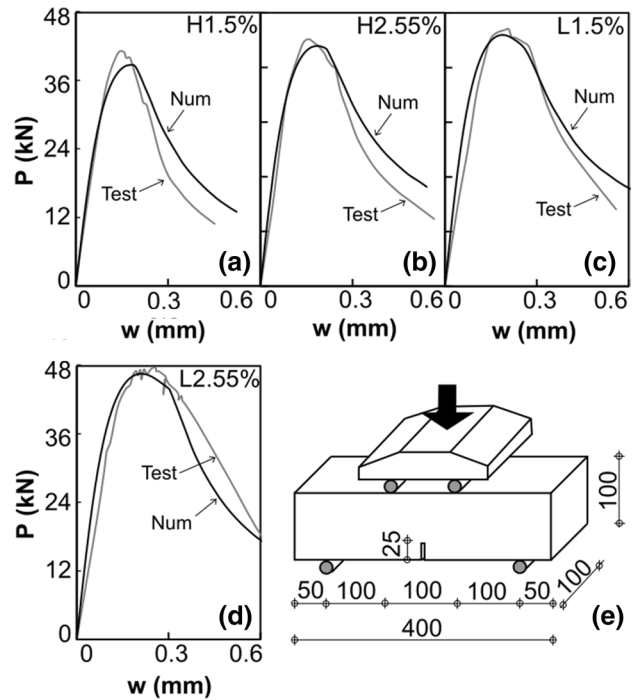

Fig. 5 Comparative assessment between test and numerical results for flexural tests: **a** H1.5%, **b** H2.55%, **c** L1.5%, **d** L2.55% concrete; **e** schematic representation of the test prisms

3.3 Numerical validation

The concrete parts of the UHPFRC beams were modelled using eight-node solid elements with reduced integration (C3D8R), whilst the longitudinal reinforcement with 3D truss elements (T3D2) [39]. The truss elements were embedded in the eight-node solid elements, and perfect bond was assumed. In contrast to the prismatic elements which had a square cross section and the numerical problem can be reduced to a plane stress case, the UHPFRC beams had an

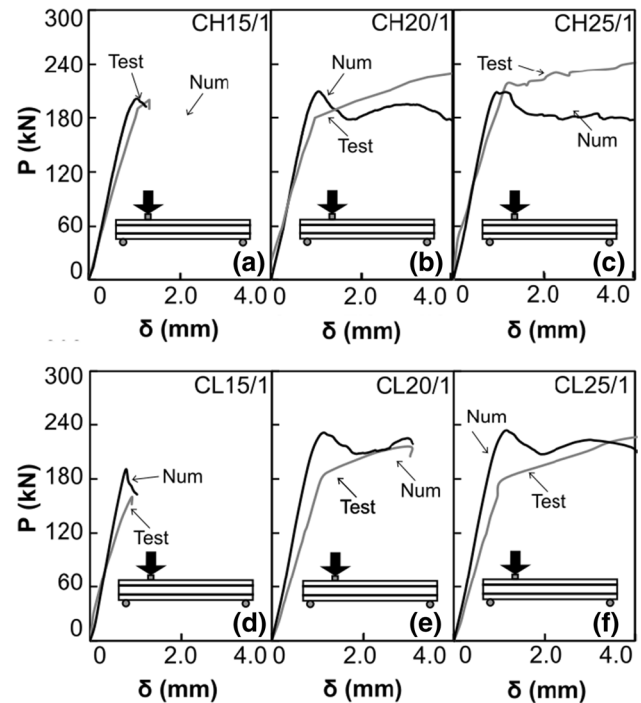**Table 4** Material parameters considered in numerical modelling

Concrete damage plasticity parameters						Steel material properties		
φ	ϵ	f_{b0}/f_c	K_c	μ	β_t/β_c	f_y	f_u	ε_u
38	0.1	1.16	0.667	1e−05	0.1/0.7	512	690	0.136

Notations: φ, dilation angle; ϵ, surface eccentricity; f_{b0}, biaxial compressive strength; f_c, uniaxial compressive strength; K_c, deviatoric plane shape factor; μ, viscosity parameter; β_t, tension recovery; β_c, compression recovery; f_y, yield strength; f_u, ultimate strength; ε_u, ultimate strain
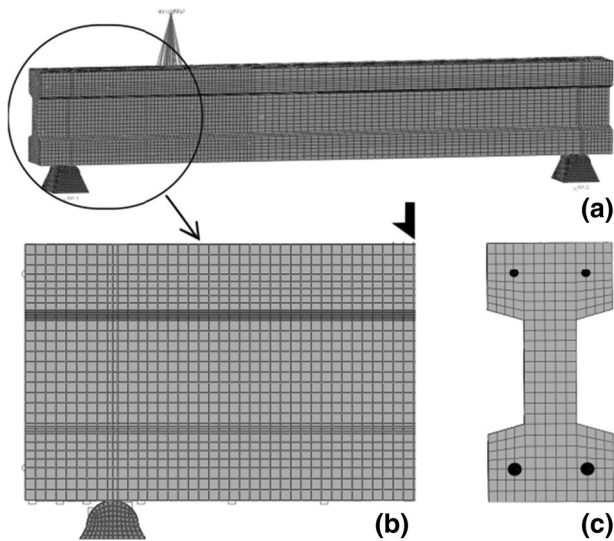
Fig. 6 Representation of the 3D beam models, **a** schematic view, **b** view of the shear span, **c** cross section

Fig. 7 Comparative assessment between the load–displacement curves for Stage 1 configurations, **a** CH15/1, **b** CH20/1, **c** CH25/1, **d** CL15/1, **e** CL20/1, **f** CL25/1

I-shaped cross section. Thus, a three-dimensional modelling was considered, primarily to capture reliably the damage propagation within the variable width of the cross section.

The 1600 mm beams were connected through two 50-mm-diameter rollers made of solid elements, representing the test boundary conditions (Fig. 6). The loading strip and the boundary rollers were tied to reference points through multi-point constraints. To simulate the test conditions, surface-to-surface interaction with tangential behaviour defined by a friction coefficient of 0.5 was assigned between rollers and concrete element. The friction confection between steel and concrete varies between 0.2 and 0.8, depending on the loading mechanism and test set-up, and values around 0.5 have been used to reliably simulate experimental tests similar to those described in this paper [e.g. 30]. The supports were assigned with elastic steel material properties, as they were overdesigned to remain in the elastic regime. As for the prismatic models, the Newton–Raphson method was used for the integration procedure and a displacement control procedure was considered in which a vertical displacement δ was applied to the relevant reference points. The gravity load was included prior to applying the vertical displacement.

The p–δ load–displacement responses obtained from the numerical simulations on the three-dimensional beam geometry illustrated in Fig. 6, for the specimens described in Sect. 2.3, are shown in Figs. 7 and 8, whilst the main parameters are given in Table 3. The displacement values shown in the figures are those measured on the opposite face to the load application point, which corresponds to notation D1 in Fig. 1. Good agreement was obtained between the predictions and test strengths with a $P_{test}/P_{num} = 1.01$ and coefficient of variation COV of 0.12 for the cases with $l_s = 1400$ mm moment span.

Using the same material properties, it is shown that the numerical strengths are slightly larger than those from the second set of tests ($l_s = 560$ mm) with a test-to-numerical average of 0.92, particularly since the test beams might have suffered micro-cracking from Stage 1 tests ($l_s = 1400$ mm). It is worth noting that steel fibres have minimal influence on the compressive strength of the material in comparison
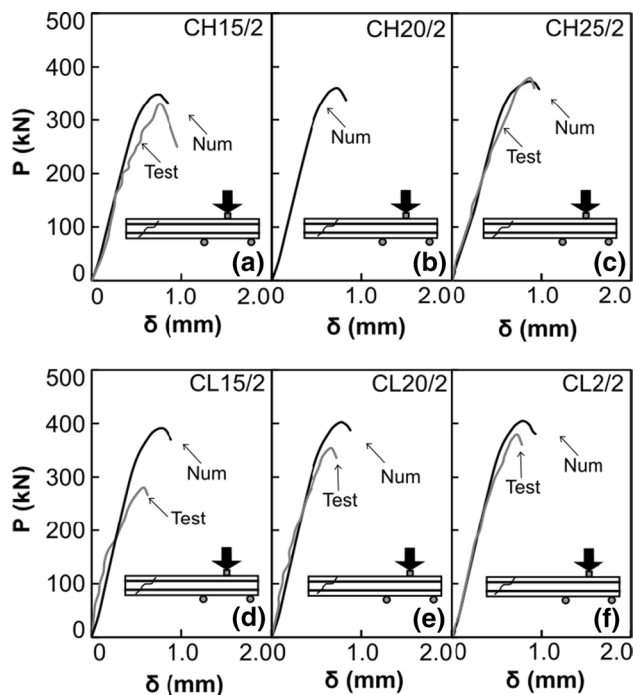
Fig. 8 Comparative assessment between the load–displacement curves for Stage 2 configurations, **a** CH15/1, **b** CH20/1 (only numerical results), **c** CH25/1, **d** CL15/2, **e** CL20/2, **f** CL25/2

with their influence on the tensile strength. Unsurprisingly, as indicated in Table 3, the changes in strength between the results obtained from modelling are relatively small. For low shear span-to-depth ratios, the shear capacity of reinforced concrete members is governed by the strut capacity and implicitly sensitive primarily to the compressive strength of the material.

The predicted strengths and tension damage patterns offer a clear insight into the governing ultimate behaviour. The P–δ plots show similar stiffnesses and sudden drops in capacity after reaching ultimate for most of the specimens, whilst the crack patterns in Fig. 2 are resembling the inclined tension plastic strain fields from Fig. 9. It is worth mentioning that such results were achieved with a relatively fine mesh within the shear span, in the range of $l_m = 10$ mm that corresponds to a l_m/h ratio of 0.04 and a mesh-independent uniaxial σ–ε input (Fig. 6).

The crack band model with constant fracture energy, in which the strain is a function of crack width and a characteristic element length l_e, was considered for the beam models [45]. For beam models, the numerical input was converted into inelastic cracking strain $\varepsilon_{ct,i}$ using the crack width values used for modelling the four-point bending tests. Following the numerical validation of the structural beams and prismatic members, a series of parametric investigations accounting for varying reinforcement ratios ρ_l and shear span-to-depth ratios a/d were conducted using the
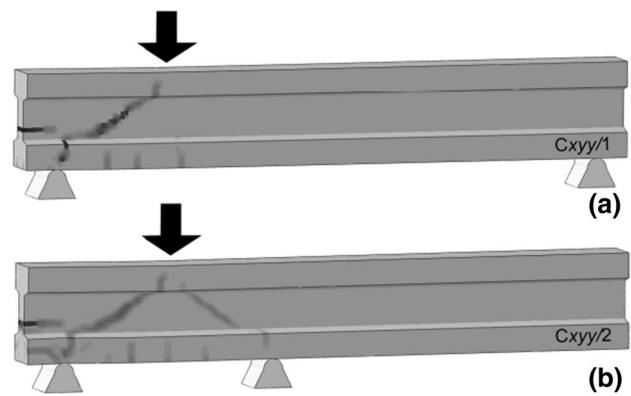
Fig. 9 Distribution of equivalent plastic strains at ultimate for: **a** Stage 1 loading scheme, **b** Stage 2 loading scheme

CDP constitutive parameters described above and listed in Table 4. An identical three-dimensional model having the same geometry and mesh as the beam models used for validations was employed for the parametric studies.

3.4 Parametric investigations

A total of 40 models incorporating four different longitudinal reinforcement ratios $\rho_l = 0.85$, 1.45, 2.00 and 2.50%, variations of the shear span-to-depth ratio $a/d = 0.75$, 1.25, 1.75, 2.25 and concrete constitutive properties of H15, H20 and H25 concrete were constructed. Model name adopts the format Cx–yyy–zzz in which x is the type of the fibre (H or L), yyy represents the shear span (e.g. 075 for $a/d = 0.75$), and zzz is for the reinforcement ratio (e.g. 145 for $\rho_l = 1.45$%). As shown in Fig. 10a, for the reduction in a/d ratio from 2.25 to 0.75, an increase in member capacity is observed, particularly due to the increase in the direct strut effect. For cases $a/d < 1.0$, it is typically assumed that the load is completely transferred to the support through the direct strut.

On the other hand, as shown in Fig. 10b, a decrease in reinforcement ratio from $\rho_l = 2.50$ to $\rho_l = 0.85$% shows a reduction in ultimate capacity and as expected a relatively more flexible response. Unsurprisingly, a low reinforcement ratio ($\rho_l = 0.85$%) combined with a high shear span-to-depth ratio $a/d = 2.25$ resulted in flexural failure. This behaviour is also captured by the tension damage fields depicted in Fig. 11. By contrast, models with $\rho_l > 2.00$% and $a/d < 1.25$ resulted in shear-governed failures, whilst for combinations of ρ_l and a/d within the above ranges developed mixed-mode failures. In terms of concrete type, it is shown that the influence in members strength is directly proportional to the input strength properties. The results and observations obtained from parametric investigations are used for the design considerations proposed in the following section, noting that only models with shear failures and $1.00 < a/d < 2.50$, representative for short a/d ratios, are considered.

Fig. 10 Numerical results: **a** influence of *a*/*d* ratio, **b** influence of reinforcement ratio to member capacity (*P*)
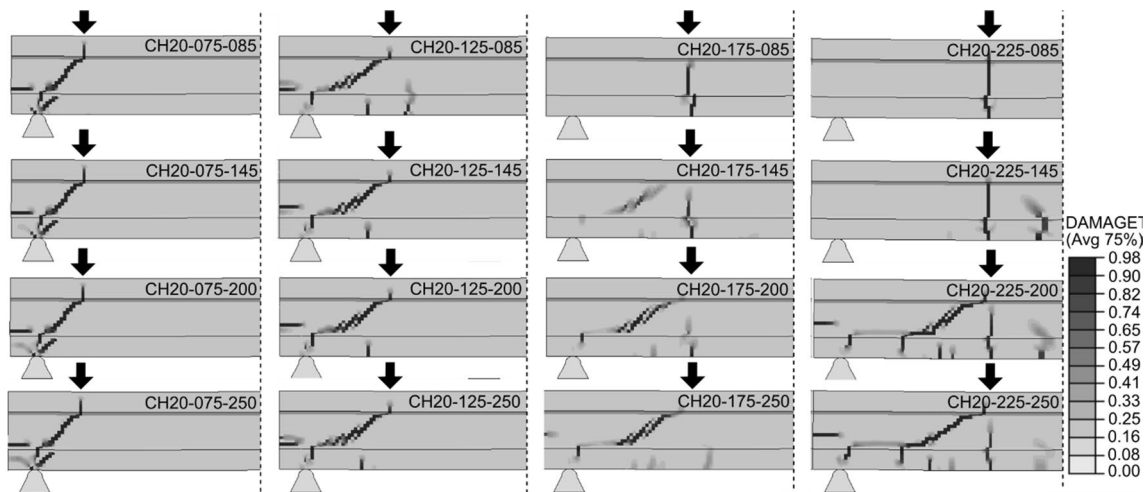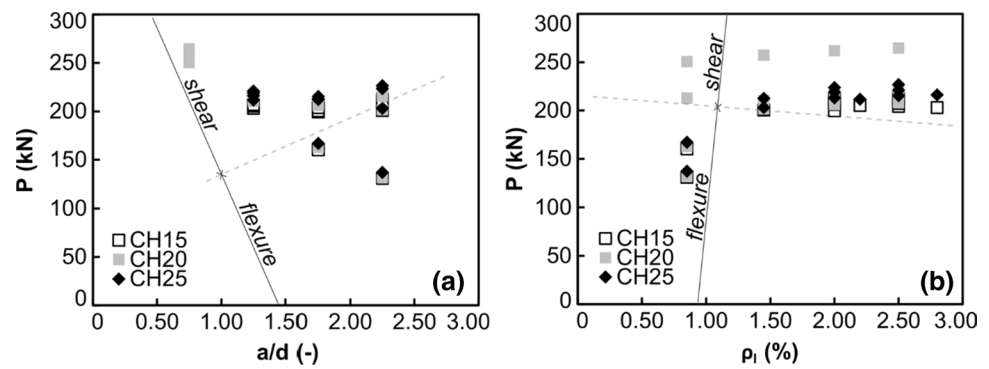
Fig. 11 Tension damage distributions at ultimate for selected models from the parametric investigations

4 Design considerations

The following section introduces a method to assess the shear strength of UHPSFRC members subjected to concentrated loads in the vicinity of the support with shear span-to-depth ratios below *a*/*d* < 2.5, using the results and observations from the tests described in Sect. 2 and numerical simulations in Sect. 3, as well as the results of a collated data set tests from the literature [46–51]. The method employs a cumulative contribution of the concrete matrix (V_c) and that of the fibres (V_f) to the total shear capacity V (Eq. 6). The contribution of the concrete matrix represented through Eq. 7 [52] is dependent on the reinforcement strain at the intersection with the critical shear crack ε, a size effect factor which depends on the maximum aggregate size (d/d_{dg}), as well as a $k = 0.019$ coefficient for the failure criterion [52]. It is worth noting, that due to the direct strut effect for members loaded within *a*/*d* < 2.5, strut-and-tie modelling can be considered in design [40, 53].

As mentioned before, the configurations investigated in this paper cover tests and numerical models with *a*/*d* < 2.5, whilst the concrete beam shear model was validated for cases in which *a*/*d* > 2.5, particularly since the theoretical strut carries a significant amount of total shear force. To account for the loads taken to the support through the direct strut, in the proposed method, the shear resistance is modified through an enhancement factor λ_β that is based on typical assumptions in codified procedures, which consider an inverse reduction β factor applied to the design shear force [40, 53]. A detailed analysis of the results of a database with simply supported beams without shear reinforcement subjected to concentrated loads showed that enhancement factors around $2.5 \times d/a$ would be appropriate and would always offer safe or overly conservative estimates, whilst $3.5 \times d/a$ would fit the average representation [54].

Additionally, current shear models were typically validated to concrete strengths below those investigated in this paper. It is also known that for concrete under uniaxial compression, the deviation from elastic stiffness occurs later for

high-strength concrete materials in comparison with normal or low strength, and this effect becomes more visible for UHPC. The latter behaves practically elastic nearly until crushing ($\sigma \approx 0.95 \times f_c$). This response would enhance the capacity of load-carrying struts that can be characterised by undisturbed uniaxial compression states. Considering the above comments, the factor employed to account for the shear enhancement due to direct strut effect near the supports is $\lambda_\beta = 3.5$ (Eq. 7b).

In terms of shear transfer actions, in conventional reinforced concrete, the forces are transferred though the compression zone, dowel action, residual stresses at the crack tip and aggregate interlock [55]. The aggregate interlock contribution is dependent on the roughness of the crack interface, aggregate type, their embedment depth in the cement paste, the magnitude of the slip and the opening of the two interfaces [16]. Several studies have shown that aggregate interlock plays a significant role as a shear carrying mechanism at low concrete compressive strengths, yet for high-strength concrete or fine powder concretes that do not contain any coarse aggregates, any contribution along cracked interfaces due to aggregate interlock, and/or shear friction, is greatly reduced [56, 57]. This is also supported by experimental evidence which showed that relatively straight cracks are characterised by smooth fracture planes and that the cracked interfaces typically pass through the aggregate particles [58]. Implicitly, in UHPC beams in shear, the aggregate interlock effect is limited or non-existent. To capture this effect, in analytical modelling the aggregate size d_g is typically taken as zero for such members [59]. The strain in the reinforcement ε_s is calculated considering the acting bending moment M_S at half shear span ($x = a/2$) from the load application point and accounts for the contribution of fibres to the moment capacity (Eqs. 7c, d). The contribution of fibres to bending capacity is averaged across the failure surface $A_{f,b}$, whilst f_f is the tensile strength provided by fibres as a product of the global orientation factor $K_{f,max}$, fibre aspect ratios α_f, fibre volume ρ_f and the bond performance of embedded fibres τ_b, described below.

$$V = V_c + V_f \tag{6}$$

$$V_c = \frac{\lambda_\beta k b_w d \sqrt{f_c}}{\sqrt{\varepsilon_s d / (16 + d_g)}} \tag{7a}$$

$$\text{where} \quad \lambda_\beta = \begin{vmatrix} 1.0 \to a_v/d > 2.5 \\ 3.5 \times (d/a_v) \to 1.0 \le a_v/d \le 2.5 \end{vmatrix} \tag{7b}$$

$$\varepsilon_s = \frac{M_S - A_{f,b} f_f (h/2)}{A_s E_s (d - c/2)} \tag{7c}$$

$$c = \frac{A_s f_y + A_{f,b} f_f}{\lambda f_c b_w}. \tag{7d}$$

In SFRC, besides the above mechanisms, the fibres bridge the crack interfaces acting as an additional strength enhancement mechanism. The shear capacity of high-performance fibre-reinforced concrete strongly depends on the amount of fibre in the concrete mixture [60]. Hence, the fibre contribution of the shear capacity depends on the fibre type, geometry, bond properties as well as the fibre orientation in the fractured plane (Eq. 8a), considering that the contribution of fibres is averaged over the failure surface [61]. The inclination of the fracture plane can be determined with Eq. 8b [16]. The global orientation factor $K_{f,max}$ is determined from the assumption that all fibres are pulled out from the matrix using a crack width dependent formulation [62]. In design, for typical fibre ranges with aspect ratios $\alpha_f = 20$–120 and diameters $d_f = 0.15$–0.90 mm, $K_{f,max}$ can be determined with Eq. 8c [57]. As expected, the bond performance τ_b of embedded fibres depends on their geometry, and as shown in Eq. 8e, it is a function of the square root of concrete strength. For hooked-end fibres, the λ_f parameter is in the range of $\lambda_f = 1.0$–1.5, whilst for straight fibres varies between $\lambda_f = 0.6$–0.9 [57, 62]. For the assessments in this paper, a nonlinear representation of λ_f, as a function of V_f is considered, in which the polynomial parameters of Eq. 8f are relevant for hooked-end fibres.

$$V_f = K_{f,max} \alpha_f \rho_f \tau_b b_w z \cot \theta \tag{8a}$$

$$\text{where} \quad \tan \theta = 0.6 + \rho_1 \frac{f_{ys}}{f_c} \left(\frac{d}{1600} \right)^{0.5} \tag{8b}$$

$$K_{f,max} = 0.5 - \left(0.645 / \alpha_f^{0.45} \right) \tag{8c}$$

$$\alpha_f = l_f / d_f \tag{8d}$$

$$\tau_b = \lambda_f \sqrt{f_c} \tag{8e}$$

$$\lambda_f = 1 - 0.05 \times V_f^2. \tag{8f}$$

Estimates of shear strength V using Eqs. 6–8 are plotted in Fig. 12a against the shear strength V_{test} of members tests from this paper and those from the collated database (Table 5) as well as the shear strength V_{num} of models from the parametric investigations in Sect. 3.3. As observed from the figure, the estimates of the proposed constitutive equations are in reasonably good agreement with the test and numerical results with an overall average of test-to-predicted V_{calc}/V_{test} ratio of 1.15 and a coefficient of variance of 0.17. The comparative results between tests in this paper and

Fig. 12 Strength predictions: **a** Eqs. (6–8), **b** model code 2010 [41]
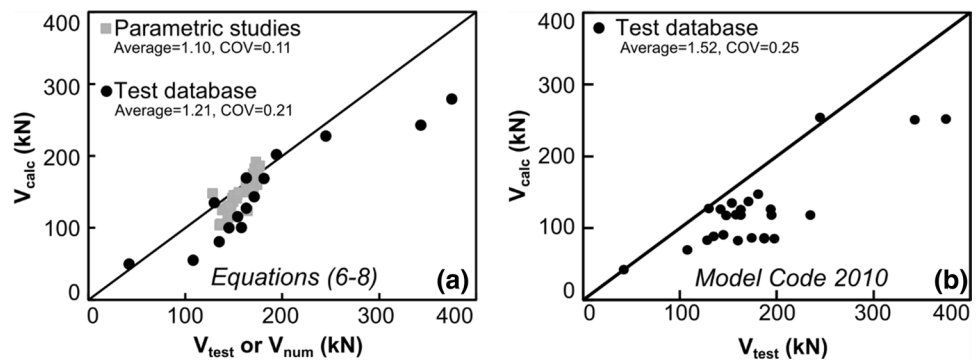
database versus predictions show a V_{calc}/V_{test} ratio of 1.21, whilst between numerical results and predictions a V_{calc}/V_{test} of 1.10, respectively. Close inspection into the predictions offered by Eqs. (6–8) and those available in the literature indicates that the former are superior to the latter which typically offer either unconservative or overly conservative estimates. As shown in Fig. 12b, predictions of the test strengths using the model available in Model Code 2010 [41], which employs at its basis the Eurocode 2 [52] fundamentals with due account for the presence of the fibres, show a V_{calc}/V_{test} ratio of 1.52 and a COV in the range of 0.25.

It is hence shown that the proposed assessment method results in relatively conservative estimates, particularly when compared with the test database and can be directly used in practice. However, it is worth noting that the predictions of the proposed expressions are limited to the ranges of the data set. For the shear span-to-depth ratios investigated in this paper, more refined results could be obtained by strut-and-tie design, provided that detailed information regarding the size of the support and load transfer plates is available. In practical design, the shear strength of a beam member is taken as the minimum between that of the sectional shear that can be assessed with Eqs. (6–8) and of that attributable to arching action can be predicted using strut-and-tie models [63].

5 Concluding remarks

The performance of ultra-high-performance steel fibre-reinforced concrete (UHPSFRC) subjected to loads at relatively low shear span-to-depth ratios was investigated in this study. The results from six UHPSFRC structural members provided with longitudinal reinforcement only, as well as corresponding material tests were reported and discussed in detail. Nonlinear numerical simulations were also carried out, and their results were compared to those from tests. The numerical models were used to carry out sensitivity studies with particular focus on the tensile constitutive response as well as the influence of key structural parameters to shear strength. The test results combined with those from numerical simulations and from a collated database from previous experimental studies enabled the development of a series of design expressions to estimate shear strength of UHPSFRC beams.

The experimental and numerical results showed that the shear strength and failure mode of such members is largely dependent on the fibre content, flexural reinforcement ratio and location of loading. An increase in hybrid fibre blend content from 1.5 to 2.0% indicated an enhancement in strength 17%, whilst an increase in fibre content from 1.5 to 2.55% showed a higher strength with about 24%, whilst previous studies indicated that from 0 to 2% the strength enhancement was twofold. More importantly, the members with higher fibre volume showed a flexurally governed shear failure, whilst those with 1.5% failed with limited or no sign of flexure. It is worth noting that similar trends were obtained from tests on flexural prisms.

The numerical simulations indicate that nonlinear models can be used to assess the tensile stress–strain curve of UHPSFRC from flexural tests as well as the strength and failure mode of structural members, provided that a refined mesh and characteristic constitutive parameters are accounted for. These showed that for the reduction in shear span-to-depth ratio from 2.25 to 0.75, an increase in capacity is observed due to the direct strut effect, whilst a reduction in the flexural reinforcement ratio shows a decrease in ultimate capacity and as expected a relatively more flexible response. Low reinforcement ratios combined with a high shear span-to-depth ratio would result in bending-governed failures, whilst high reinforcement ratios combined with short loaded spans would produce shear-governed failures. Considering the range of parameters accounted for in the parametric assessments along with those from the collated database, the expressions proposed offer a reliable design method and suitable for practical application.

Table 5 Database and predictions

References	ID	b_w or b (mm)	d (mm)	l_s (mm)	ρ_1 (%)	a/d (−)	d_g (mm)	f_c (MPa)	V_f (%)	Fibre type*	V_{test} (kN)	V_{test}/V_{calc} (−)
This paper	CH15/1	60	223	1400	1.15	1.25	1.2	135.7	1.50	$H+S$	160	1.18
	CH20/1	60	223	1400	1.15	1.25	1.2	150.0	2.00	$H+S$	187	1.22
	CH25/1	60	223	1400	1.15	1.25	1.2	147.7	2.50	$H+S$	198	1.26
	CL15/1	60	223	1400	1.15	1.25	1.2	138.2	1.50	H	128	0.87
	CL20/1	60	223	1400	1.15	1.25	1.2	155.0	2.00	H	174	1.09
	CL25/1	60	223	1400	1.15	1.25	1.2	153.6	2.50	H	187	1.15
Manju et al. [46]	SH1	140	175	2000	1.28	1.50	12	82.0	0.50	H	148	1.19
	SH2	140	175	2000	1.28	1.50	12	83.2	1.00	H	195	1.20
	SH3	140	175	2000	1.28	1.50	12	83.8	1.50	H	235	1.21
Spinella et al. [47]	B10	150	219	2300	1.91	2.00	10	80.0	1.00	H	142	0.92
Ashour et al. [48]	B-1-0.5-A	125	215	930	2.83	1.00	10	99.0	0.50	H	245	1.08
	B-1-1.0-A	125	215	930	2.83	1.00	10	95.3	1.00	H	343	1.41
	B-1-1.5-A	125	215	930	2.83	1.00	10	96.4	1.50	H	375	1.34
	B-2-0.5-A	125	215	1360	2.83	2.00	10	99.1	0.50	H	130	0.96
	B-2-1.0-A	125	215	1360	2.83	2.00	10	95.3	1.00	H	163	0.96
	B-2-1.0-M	125	215	1360	4.58	2.00	10	94.5	1.00	H	181	1.07
	B-2-1.5-A	125	215	1360	2.83	2.00	10	96.6	1.50	H	194	0.96
Bae et al. [49]	U-0-f-2.0	200	300	1200	3.60	2.00	2.0	199.0	2.00	H	587	1.02
Cho and Kim [50]	F80-0.5-16	120	167	720	2.00	1.43	13	82.4	0.50	H	158	1.57
	F80-0.5-19	120	167	720	2.82	1.43	13	86.1	0.50	H	154	1.33
	F80-1.0-16	120	167	720	2.00	1.43	13	81.1	1.00	H	163	1.28
	F80-1.0-19	120	167	720	2.82	1.43	13	89.4	1.00	H	171	1.19
Kwak et al. [51]	FHB2-2	125	212	1248	1.52	2.00	19	63.8	0.50	H	135	1.67
	FNB2-2	125	212	1248	1.52	2.00	19	30.8	0.50	H	108	1.97
	FHB3-2	125	212	1248	1.52	2.00	19	68.6	0.75	H	145	1.45
Tahenmi et al. [64]	S0F0.5-65	100	135	900	1.16	2.22	15	64.2	0.50	H	42	0.84

*$H+S$, hooked end and straight; H, hooked end; notations: b_w, web thickness; b, beam width; d, effective bending depth; d, effective bending depth; l_s, moment span; ρ_1, reinforcement ratio; a/d, shear span-to-depth ratio; d_g, aggregate size; f_c, concrete compressive strength; V_{test}, test strength; V_{calc}, assessed strength with Eqs. (6–8)

References

1. Sobuz HR, Visintin P, Ali MM, Singh M, Griffith MC, Sheikh AH. Manufacturing ultra-high performance concrete utilising conventional materials and production methods. Constr Build Mater. 2016;111:251–61. https://doi.org/10.1016/j.conbuildmat.2016.02.102.

2. Randl N, Steiner T, Ofner S, Baumgartner E, Mészöly T. Development of UHPC mixtures from an ecological point of view. Constr Build Mater. 2014;67:373–378.5. https://doi.org/10.1016/j.conbuildmat.2013.12.102.

3. Han B, Dong S, Ou J, Zhang C, Wang Y, Yu X, Ding S. Microstructure related mechanical behaviors of short-cut super-fine stainless wire reinforced reactive powder concrete. Mater Des. 2016;96:16–26. https://doi.org/10.1016/j.matdes.2016.02.004.

4. Groli G, Pérez Caldentey A, Soto AG. Cracking performance of SCC reinforced with recycled fibres—an experimental study. Struct Concr. 2014;15(2):136–53. https://doi.org/10.1002/suco.201300008.

5. Minelli F, Plizzari GA. On the effectiveness of steel fibers as shear reinforcement. ACI Struct J. 2013;110(3):379–89.

6. Magureanu C, Sosa I, Negrutiu C, Heghes B. Mechanical properties and durability of ultra-high-performance concrete. ACI Mater J. 2012;109(2):177.

7. Yang SL, Millard SG, Soutsos MN, Barnett SJ, Le TT. Influence of aggregate and curing regime on the mechanical properties of ultra-high performance fibre reinforced concrete (UHPFRC). Constr Build Mater. 2009;23(6):2291–8. https://doi.org/10.1016/j.conbuildmat.2008.11.012.

8. Dugat J, Roux N, Bernier G. Mechanical properties of reactive powder concretes. Mater Struct. 1996;29(4):233–40. https://doi.org/10.1007/bf02485945.

9. Ma J, Schneider H. Properties of ultra-high-performance concrete. Leipzig Ann Civ Eng Rep (LACER). 2002;7:25–32.

10. Yu R, Spiesz PHJH, Brouwers HJH. Development of an eco-friendly ultra-high performance concrete (UHPC) with efficient cement and mineral admixtures uses. Cem Concr Compos. 2015;55:383–94. https://doi.org/10.1016/j.cemconcomp.2014.09.024.

11. Hassan AMT, Jones SW, Mahmud GH. Experimental test methods to determine the uniaxial tensile and compressive behaviour of ultra high performance fibre reinforced concrete (UHPFRC). Constr Build Mater. 2012;37:874–82. https://doi.org/10.1016/j.conbuildmat.2012.04.030.

12. Di Prisco M, Plizzari G, Vandewalle L. Fibre reinforced concrete: new design perspectives. Mater Struct. 2009;42(9):1261–81. https://doi.org/10.1617/s11527-009-9529-4.

13. Krahl PA, Gidrão GDMS, Carrazedo R. Cyclic behavior of UHPFRC under compression. Cem Concr Compos. 2019;103:363. https://doi.org/10.1016/j.cemconcomp.2019.103363.

14. Rossi P. Influence of fibre geometry and matrix maturity on the mechanical performance of ultra high-performance cement-based composites. Cem Concr Compos. 2013;37:246–8. https://doi.org/10.1016/j.cemconcomp.2012.08.005.

15. Kwak YK, Eberhard MO, Kim WS, Kim J. Shear strength of steel fiber-reinforced concrete beams without stirrups. ACI Struct J. 2002;99(4):530–8.

16. Bompa DV, Elghazouli AY. Ultimate shear behaviour of hybrid reinforced concrete beam-to-steel column assemblages. Eng Struct. 2015;101:318–36. https://doi.org/10.1016/j.engstruct.2015.07.033.

17. Kang THK, Kim W, Kwak YK, Hong SG. Shear testing of steel fiber-reinforced lightweight concrete beams without web reinforcement. ACI Struct J. 2011;108(5):553–61.

18. Yoo DY, Yoon YS. Structural performance of ultra-high-performance concrete beams with different steel fibers. Eng Struct. 2015;102:409–23. https://doi.org/10.1016/j.engstruct.2015.08.029.

19. Singh M, Sheikh AH, Ali MM, Visintin P, Griffith MC. Experimental and numerical study of the flexural behaviour of ultra-high performance fibre reinforced concrete beams. Constr Build Mater. 2017;138:12–25. https://doi.org/10.1016/j.conbuildmat.2017.02.002.

20. Chen S, Zhang R, Jia LJ, Wang JY. Flexural behaviour of rebar-reinforced ultra-high-performance concrete beams. Mag Concr Res. 2018;70(19):997–1015. https://doi.org/10.1680/jmacr.17.00283.

21. Hasgul U, Turker K, Birol T, Yavas A. Flexural behavior of ultra-high-performance fiber reinforced concrete beams with low and high reinforcement ratios. Struct Concr. 2018;19(6):1577–90. https://doi.org/10.1002/suco.201700089.

22. Wu P, Wu C, Liu Z, Hao H. Investigation of shear performance of UHPC by direct shear tests. Eng Struct. 2019;183:780–90. https://doi.org/10.1016/j.engstruct.2019.01.055.

23. Xia J, Mackie KR, Saleem MA, Mirmiran A. Shear failure analysis on ultra-high performance concrete beams reinforced with high strength steel. Eng Struct. 2011;33(12):3597–609. https://doi.org/10.1016/j.engstruct.2011.06.023.

24. Qi JN, Ma ZJ, Wang JQ, Liu TX. Post-cracking shear strength and deformability of HSS-UHPFRC beams. Struct Concr. 2016;17(6):1033–46. https://doi.org/10.1002/suco.201500191.

25. Zagon R, Matthys S, Kiss Z. Shear behaviour of SFR-UHPC I-shaped beams. Constr Build Mater. 2016;124:258–68. https://doi.org/10.1016/j.conbuildmat.2016.07.075.

26. Barros JA, Cunha VM, Ribeiro AF, Antunes JAB. Post-cracking behaviour of steel fibre reinforced concrete. Mater Struct. 2005;38(1):47–56. https://doi.org/10.1007/BF02480574.

27. Kang ST, Lee Y, Park YD, Kim JK. Tensile fracture properties of an ultra high performance fiber reinforced concrete (UHPFRC) with steel fiber. Compos Struct. 2010;92(1):61–71. https://doi.org/10.1016/j.compstruct.2009.06.012.

28. Krahl PA, Carrazedo R, El Debs MK. Mechanical damage evolution in UHPFRC: experimental and numerical investigation. Eng Struct. 2018;170:63–77. https://doi.org/10.1016/j.engstruct.2018.05.064.

29. Zingaila T, Augonis M, Arruda MRT, Šerelis E, Kelpša Š. Experimental and numerical analysis of flexural concrete-UHPFRC/

RC composite members. Mechanics. 2017;23(2):182–9. https://doi.org/10.5755/j01.mech.23.2.17210.

30. Moharram MI, Bompa DV, Elghazouli AY. Experimental and numerical assessment of mixed RC beam and steel column systems. J Constr Steel Res. 2017;131:51–67. https://doi.org/10.1016/j.jcsr.2016.12.019.

31. CEN (European Committee for Standardization) EN 197-1:2011 Cement. Composition, specifications and conformity criteria for common cements, CEN, Brussels (Belgium); 2011.

32. SikaFume—additive for durable and high-ultimate-strength concrete—datasheed. https://aus.sika.com/dms/getdocument.get/4f26fc3a-352c-317d-b68d-6ac5ec83065d/SikaFume-en-AU-(02-2018)-1-1.pdf. Accessed 4 Aug 2019.

33. BASF—MasterGlenium ACE 440 datasheet. https://assets.master-builders-solutions.basf.com/it-it/basf-masterglenium%20ace%20440%20oct_2016%20en.pdf. Accessed 4 Aug 2019.

34. Baumbach metal—steel fibres for concrete reinforcement. https://www.baumbach-metall.de/cms/upload/Prospekte/Prospekt_allgemein_betonbewehrung.pdf (in German).

35. Krampeharex—wire fibre data sheet. https://www.krampeharex.com/typo3temp/pdf/PDB_KrampeHarex-wire-fibre-DM_6_0_175.pdf?1557991886. Accessed 4 Aug 2019.

36. Magureanu C, Sosa I, Negrutiu C, Heghes B. Bending and shear behavior of ultra-high performance fiber reinforced concrete. High Perform Struct Mater V. 2010;112:79.

37. Wang Z, Hu H, Hajirasouliha I, Guadagnini M, Pilakoutas K. Tensile stress–strain characteristics of rubberised concrete from flexural tests. Constr Build Mater. 2020;236:117591. https://doi.org/10.1016/j.conbuildmat.2019.117591.

38. Uchida Y, Rokougo K, Koyanagi W. Determination of tension softening curves of concrete by means of bending tests. In: *ECF8, Torino*; 1990.

39. DSS (Dassault Systèmes Simulia Corp). ABAQUS analysis user's manual 6.14-2; 2014.

40. Sakr MA. Effect of cyclic loadings on the shear strength and reinforcement slip of RC beams. Civ Eng J. 2017;3(2):111–23. https://doi.org/10.28991/cej-2017-00000078.

41. fib—Fédération internationale du béton. Model Code 2010—final draft, vols. 1–2, fib Bulletins 65–66, Lausanne (Switzerland); 2012.

42. Hordijk DA. Local approach to fatigue of concrete. Doctorate dissertation. Delft: Delft University of Technology; 1991.

43. Wosatko A, Pamin J, Polak MA. Application of damage–plasticity models in finite element analysis of punching shear. Comput Struct. 2015;151:73–85. https://doi.org/10.1016/j.compstruc.2015.01.008.

44. Graybeal B, Davis M. Cylinder or cube: strength testing of 80 to 200 MPa (11.6 to 29 ksi) ultra-high-performance fiber-reinforced concrete. ACI Mater J. 2008;105(6):603.

45. Bažant ZP, Oh BH. Crack band theory for fracture of concrete. Matér Constr. 1983;16(3):155–77. https://doi.org/10.1007/BF02486267.

46. Manju R, Sathya S, Sylviya B. Shear strength of high-strength steel fibre reinforced concrete rectangular beams. Int J Civ Eng Technol (IJCIET). 2017;8(8):1716–29.

47. Spinella N, Colajanni P, La Mendola L. Nonlinear analysis of beams reinforced in shear with stirrups and steel fibers. ACI Struct J. 2012;109(1):53.

48. Ashour SA, Hasanain GS, Wafa FF. Shear behavior of high-strength fiber reinforced concrete beams. ACI Struct J. 1992;89(2):176–84.

49. Bae BI, Choi HK, Choi CS. Flexural and shear capacity evaluation of reinforced ultra-high strength concrete members with steel Rebars. In: Key engineering materials, vol. 577; 2014, pp. 17–20. https://doi.org/10.4028/www.scientific.net/KEM.577-578.17.

50. Cho SH, Kim YI. Effects of steel fibers on short beams loaded in shear. ACI Struct J. 2003;100(6):765–74.

51. Kwak KH, Suh J, Hsu CTT. Shear-fatigue behavior of steel fiber reinforced concrete beams. ACI Struct J. 1991;88(2):155–60.

52. Cavagnis F, Ruiz MF, Muttoni A. A mechanical model for failures in shear of members without transverse reinforcement based on development of a critical shear crack. Eng Struct. 2018;157:300–15. https://doi.org/10.1016/j.engstruct.2015.09.015.

53. CEN (European Committee for Standardization). EN 1992-1-1. Eurocode 2: design of concrete structures—part 1-1: general rules and rules for buildings Brussels; 2004.

54. Jacobs JP. Commentary to Eurocode 2. Brussels: European Concrete Platform ASBL; 2008. p. 168.

55. Huber P, Huber T, Kollegger J. Investigation of the shear behavior of RC beams on the basis of measured crack kinematics. Eng Struct. 2016;113:41–58. https://doi.org/10.1016/j.engstruct.2016.01.025.

56. Mphonde AG. Aggregate interlock in high strength reinforced concrete beams. Proc Inst Civ Eng. 1988;85(3):397–413. https://doi.org/10.1680/iicep.1988.444.

57. Voo YL, Poon WK, Foster SJ. Shear strength of steel fiber-reinforced ultrahigh-performance concrete beams without stirrups. J Struct Eng. 2010;136(11):1393–400. https://doi.org/10.1061/(ASCE)ST.1943-541X.0000234.

58. Hamrat M, Boulekbache B, Chemrouk M, Amziane S. Shear behaviour of RC beams without stirrups made of normal strength and high strength concretes. Adv Struct Eng. 2010;13(1):29–41. https://doi.org/10.1260/1369-4332.13.1.29.

59. Angelakos D, Bentz EC, Collins MP. Effect of concrete strength and minimum stirrups on shear strength of large members. ACI Struct J. 2001;98(3):291–300.

60. Pansuk W, Nguyen TN, Sato Y, Den Uijl JA, Walraven JC. Shear capacity of high performance fiber reinforced concrete I-beams. Constr Build Mater. 2017;157:182–93. https://doi.org/10.1016/j.conbuildmat.2017.09.057.

61. Ng TS, Amin A, Foster SJ. The behaviour of steel-fibre-reinforced geopolymer concrete beams in shear. Mag Concr Res. 2013;65(5):308–18. https://doi.org/10.1680/macr.12.00081.

62. Voo JYL, Foster SJ. Variable engagement model for the design of fibre reinforced concrete structures. In: Proceedings advanced materials for construction of bridges, buildings, and other structures III. ECI Digital Archives; 2003.

63. Sagaseta J, Vollum RL. Shear design of short-span beams. Mag Concr Res. 2010;62(4):267–82. https://doi.org/10.1680/macr.2010.62.4.267.

64. Tahenni T, Chemrouk M, Lecompte T. Effect of steel fibers on the shear behavior of high strength concrete beams. Constr Build Mater. 2016;105:14–28. https://doi.org/10.1016/j.conbuildmat.2015.12.010.